An Investigation of Continuous and Discontinuous Finite-Element Discretizations on Benchmark 3D Turbulent Flows (Invited)

Behzad R. Ahrabi,[1] Michael J. Brazell,[2] and Dimitri J. Mavriplis[3]

Department of Mechanical Engineering, University of Wyoming, Laramie, WY 82071

Two high-order finite-element solvers are used to simulate two 3D benchmark problems provided by the NASA Turbulence Modeling Resource (TMR) website. The first problem is a subsonic turbulent flow over a hemisphere-cylinder body at angles of attack of 5 and 19 degrees. The second problem is a transonic turbulent flow over an ONERA M6 wing at angles of attack of 3.06 and 6.06 degrees. The first finite-element solver is based on the streamline-upwind Petrov-Galerkin (SUPG) discretization and the second one is based on the discontinuous Galerkin (DG) method. For both problems, second- and higher-order solutions are provided and a detailed mesh convergence study is presented. Also, the linear and nonlinear convergence behavior of the utilized solvers is investigated. The SUPG solver shows a very consistent non-linear convergence behavior across all grids while the DG solver struggles on the coarse grids. Both finite-element solvers demonstrate rapid convergence for high-order simulations when initialized with a second-order accurate solution. For all hemisphere-cylinder cases and the M6 wing at angle of attack of 3.06 degrees, the finite-element solvers are outperforming the FUN3D finite-volume solver in terms of accuracy per degree of freedom. For the M6 wing at angle of attack of 6.06 degrees, although no reference solutions were provided by the TMR website, simulations were attempted for the finite-element solvers. For this case, no conclusions can be made about asymptotic convergence of the integrated forces due to lack of consistency between results. This was initially thought to be caused by the provided grids. However, further investigation using custom unstructured grids leads us to believe that the flow conditions, not the grids, make this case challenging.

I. Introduction

The field of computational fluid dynamics (CFD) continues to grow rapidly partly due to the ever-increasing access to computational resources. As a result, existing and developing CFD solvers are being used on more complex and larger simulations than before. As new discretizations are being developed in effort to increase the accuracy and efficiency over more established discretizations, standardized test cases are required to assess the performance of the new discretizations. In addition, having a set of standard test problems allows for confirming the implementation correctness and comparing the accuracy between discretizations. The Turbulence Modeling Resource (TMR) website [1] maintained by NASA Langley research center provides detailed descriptions on how to implement various turbulence and transition models. This website also provides a variety of validation and verification test cases ranging from simple two-dimensional flat plates to computationally challenging three-dimensional aircraft wings. These cases include detailed descriptions of flow conditions, boundary conditions, grids, and reference results. The database include experimental data as well

[1]AIAA Senior Member, Associate Research Scientist, brezaahr@uwyo.edu

[2]AIAA Member, Associate Research Scientist, mbrazell@uwyo.edu

[3]AIAA Associate Fellow, Professor, mavripl@uwyo.edu

as numerical solutions from NASA codes such as CFL3D [2, 3], USM3D [4, 5], and FUN3D [6-9]. A special session on solver technology for turbulent flows was held at the AIAA Science and Technology Forum and Exposition (SciTech) conference in 2015 [10-17]. This session focused on the NACA 0012 airfoil and led to a Special Section on Evaluation of RANS Solvers on Benchmark Aerodynamics Flows in the AIAA journal [18-22]. In 2016, another special session at SciTech was held focusing on more difficult cases such as a subsonic flow over a 3D bump, a supersonic flow in a 3D square duct, and a subsonic flow over a 3D hemisphere cylinder at zero angle of attack [23-27].

For the 2018 SciTech conference, the special session on the solver technology will focus on the 3D hemisphere cylinder at multiple angles of attack and the ONERA M6 wing at two angles of attack. The focus of this paper will be on finite-element simulations of these two problems using a streamline-upwind Petrov-Galerkin (SUPG) method and a discontinuous Galerkin (DG) method. High-order finite-element discretizations have shown success in the past on the simpler test cases. It is clear now that for smooth solutions high-order methods can obtain more accurate solutions with fewer degrees of freedom compared to lower-order methods. High-order methods have also contributed in many enhancements to non-linear and linear solvers. As a result, convergence of the residuals to the machine-zero has become common in the high-order community. However, it is not clear if the enhancements in linear and nonlinear solution strategies have led to more efficient algorithms in terms of memory consumption and computational cost. In an effort to be transparent about the performance of these methods non-linear convergence will be provided showing both successful runs and some difficulties encountered. We also attempt to compare and contrast the two finite-element methods in this work.

The remainder of this paper is organized as follows: first we describe the capabilities of the two finite-element discretizations used in this work. Next, we describe the 3D hemisphere-cylinder case, grids, and provide comparisons of the aerodynamical forces and maximum eddy viscosity to the finite-volume and finite-element solutions of the FUN3D code. Also, we provide a discussion of the non-linear converge history and make comparisons between the solvers. Similarly, the ONERA M6 case will also be described and compared to the same FUN3D solvers and our finite-element solvers. Lastly, some conclusions will be made about accuracy and convergence behaviors of the utilized finite-element solvers.

II. Description of the Flow Solvers

A. HOMA (Stabilized Finite-Element Flow Solver)

The HOMA (High-Order Multilevel Adaptive) was introduced in Refs. [28, 29]. In this flow solver, the compressible Reynolds averaged Navier-Stokes (RANS) equations are discretized using a Petrov-Galerkin finite-element method. The lowest polynomial space is constructed using the Lagrange linear basis functions, and the higher-order spaces are built using the high-order Lagrange basis functions or a set of hierarchical basis functions. The solver is capable of handling two- and three-dimensional unstructured curved meshes with mixed element types. The time integration for steady-state and unsteady problems is fully implicit and the linearization is done exactly using the automatic differentiation (AD) technique. Unsteady problems are solved using the second-order backward difference formula (BDF2) scheme. For steady-state problems, a preconditioned Newton-Krylov method based on pseudo-transient continuation (PTC) [30, 31], and a non-linear p-multigrid method based on the full approximation scheme (FAS) are used. For preconditioning of the linear systems, incomplete lower upper factorization with arbitrary levels of fill (ILU(k)), implicit line smoothers, and Additive Schwarz methods with various local solvers have been developed as the built-in options of the code.

B. DG3D (Discontinuous Galerkin Flow Solver)

DG3D is a discontinuous Galerkin flow solver. The solver can handle hybrid mixed element meshes, curved elements, and incorporates both p-enrichment and h-refinement capabilities using non-conforming elements. It is used to discretize the compressible Navier-Stokes equations as well a PDE-based artificial viscosity equation [32, 33] and the negative-SA variant of the Spalart-Allmaras turbulence model [34]. The advective fluxes are calculated using a Riemann solver. Implemented Riemann solvers include: Lax-Friedrichs [35], Roe [36], and artificially upstream flux vector splitting scheme (AUFS) [37]. In this work, only Lax-Friedrichs flux is used. The diffusive fluxes are handled using a symmetric interior penalty (SIP) method [38, 39]. The time derivative can be approximated using the explicit scheme RK4 or an implicit BDF2 scheme. The implicit solver uses a Newton-Raphson method with PTC to solve the non-linear set of equations. These equations are linearized to obtain the full Jacobian. The linear system is solved using a flexible-GMRES [40] (fGMRES) method. To further improve convergence of fGMRES a right preconditioner can be applied to the system of equations. Preconditioners that have been implemented include Jacobi relaxation, Gauss-Seidel relaxation, line implicit Jacobi, and ILU(0). This solver has been used to successfully to solve hypersonic flows [41], turbulent flow over wings [13] and aircraft, Direct Numerical Simulations (DNS) of Taylor Green Vortex, and overset simulations [42].

III. Solution Algorithm

All the problems in this paper are solved using a preconditioned Newton-Krylov method based on the pseudo-transient continuation (PTC) [30, 31]. The details of the implementation for the HOMA and DG3D solvers can be found in Refs. [25, 28, 29]. The tolerance of the linear systems is set to 10^{-3} and 10^{-5} for HOMA and DG3D, respectively. Both solvers use the implicit line Jacobi method for preconditioning of the fGMRES linear solver. HOMA uses a dual-CFL strategy for stabilizing the preconditioner at high CFL numbers [28, 29].

IV. Subsonic Turbulent Flow over a Hemisphere-Cylinder Configuration

The first test case investigated is turbulent flow over a smooth body of revolution. This configuration consists of a cylinder capped at the nose with a hemisphere. For comparison and verification, the TMR website has provided various computational grids and corresponding numerical results from multiple NASA finite-volume and finite-element flow solvers. The provided cases were produced using the negative variant of the SA turbulence model and satisfy the same boundary conditions, which are explained in the following subsection.

A. Problem Description

Figure 1 shows the computational domain and boundary conditions of this test case. The diameter and length of the cylinder are 1.0 and 9.5 respectively. The spherical outer boundary has been placed at a distance of 100 units away from the body. The symmetry plane is located at $y = 0$. The TMR website has provided the data for angles of attack of $0^o, 5^o, 10^o, 15^o, 19^o$. For all angles, the Mach number is 0.6, the Reynolds is 0.35 million, and the reference temperature is 540^oR. Also, the Prandtl and turbulent Prandtl numbers are 0.72 and 0.9, respectively.

For both solvers used this in study, the solution is initialized by the free stream conditions. On the solid boundaries, the no-slip and adiabatic conditions are enforced weakly. Also, for both solvers, the far-field boundary conditions are applied by integration of the Roe fluxes, which are calculated based on the solution values at the interior side and the free-stream values at the outer side. For HOMA, the symmetry conditions

are applied strongly by setting the y-velocities to zero, whereas for the DG3D, the symmetry boundary is treated as an inviscid wall. For both solvers, a constant free-stream pressure is enforced at the outflow boundary condition.

B. Computational Grids and Curving Strategy

The computational grids for this test case are generated using the grid generator and grid coarsening codes provided by the TMR website. To provide a series of uniformly refined grids for grid convergence studies, first, the finest grid of the series is generated using the recommended input file in the website. This grid includes 256 elements along the cylinder, 64 elements along the hemisphere, and 1280 elements in the radial direction. The spacing normal to the wall is such that a $y^+ = 0.5$ is targeted. Then, the provided coarsening code is recursively used to remove the vertices from each input grid. By doing this, the finer grids are all nested in the coarser ones. The grid generator code is able to generate five families of grids:

1. Unstructured with prismatic elements
2. Unstructured with tetrahedral elements
3. Unstructured with mixed prismatic and tetrahedral elements
4. Unstructured with mixed prismatic and hexahedral elements
5. Structured with hexahedral elements and prismatic elements at the polar singularity

For most studied cases, the continuous and discontinuous solvers are utilized on different grids as described below. In the following discussion, P represents the polynomial degree of the solution space, and Q represents the polynomial degree of the geometrical mapping.

The continuous solver is run on iso-parametric ($Q = P$) grids from the second and forth families. To curve the high-order grids, the removed vertices from the finer grids in the series are used. To facilitate this, during the coarsening process, the coarsening code saves the coordinates of the removed vertices from each element. Figure 1c shows an example of a tetrahedral grid curved using this approach.

The discontinuous solver is run on iso-parametric grids from the second family and super-parametric ($Q = P + 1$) grids from the fifth family. As will be shown in the result section, the super-parametric elements are required for the discontinuous Galerkin method to obtain the nominal accuracy order of accuracy. To achieve the $P + 1$ curvature, the mesh is curved using the analytic definition of the geometry. To apply this curvature, the elements surrounding the hemisphere-cylinder are first initialized using straight-sided elements. Then the straight-sided elements are used to project equidistant points including the original corner nodes of the element (the number of points is equal to the number of mapping basis functions). The points on the corners of the elements already satisfy the analytic formula, while the remaining nodes are perturbed on the boundary face to satisfy this formula. This perturbation is pushed to the other nodes on the element in the normal direction. A Vandermonde matrix is created and used to solve for the modal coefficients used in the mapping basis. This curvature is then pushed outward in the normal direction along the cell-based lines from the surface to neighboring elements. This process is repeated for every element on the boundary.

The coarsening code with the recommended input produces 7 grids for all the grid families. In each series, the grid 1 is the finest grid and the grid 7 is the coarsest one. Tables 1 and 2 show the statistics of the utilized grids for both solvers in this study. In these tables, the empty places correspond to the cases that have been not been run.

Table 1. Statistics of the utilized HC grids for the stabilized finite-element solver

Grids	Family 2 (Tet)			Family 4 (Hex/Prism)	
	Elements	P1 DOFs	P2 DOFs	Elements	P1 DOFs
2	53,084,169	8,995,153	-	9,830,400	8,995,153
3	6,635,520	1,143,081	8,995,153	1,228,800	1,143,081
4	829,440	147,637	1,143,081	153,600	147,637
5	103,680	-	147,637	-	-

Table 2. Statistics of the utilized HC grids for the discontinuous Galerkin solver

Grids	Family 2 (Tet)		Family 5 (Hex/Prism)			
	Elements	P1 DOFs	Elements	P1 DOFs	P2 DOFs	P3 DOFs
3	6,635,520	26,542,080	1,228,800	9,799,680	33,039,360	-
4	829,440	3,317,760	153,600	1,221,120	4,112,640	-
5	103,680	414,720	19,200	151,680	509,760	1,205,760

C. Wall Distance

The wall distance for this simulation is calculated based on the analytical definition of the geometry. For elements near the wall the curvature of the mesh does not exactly represent the geometry, this is because the mapping is defined by polynomials and the geometry is defined by a cylinder and hemisphere. For these elements, the analytic wall distance could be negative or inaccurate. To fix these problematic cells, the wall distance is calculated on equidistant points on the element (the number of points is equal to the number of mapping basis functions), a Vandermonde matrix is created and used to solve for a set of coefficients to represent the wall distance, and lastly the wall distance is projected onto the quadrature points.

D. Grid Convergence Results

Here, we discuss grid convergence of the aerodynamic forces and maximum eddy viscosity values for both finite-element solvers and compare them to the FUN3D solver results. As mentioned earlier, for this case, the TMR website provides data for angles of attack of $0^o, 5^o, 10^o, 15^o, 19^o$. Although we have successfully simulated at all angles of attack, for brevity, we only present the results of angles of attack of 5^o and 19^o degrees. Figure 2 shows the visualization of the flow for these angles. We have previously studied the angle of attack of 0^o using the discontinuous Galerkin solver in Ref. [25].

Figure 3 shows the grid convergence plots of the different flow solvers at 5^o angle of attack. In this figure, the aerodynamic forces and maximum eddy viscosity are compared on different grids and at different discretization orders. FUN3D results, for both FV and FE discretizations, are shown on the tetrahedral grids. These results are both based on the second-order accurate discretizations. FUN3D FE results are labeled by SFE (Stabilized Finite Element). The HOMA results are also shown for the tetrahedral grids at P1Q1 and P2Q2. The DG3D results are shown for the tetrahedral grids at P1Q1, and for the structured grids at P1Q2, P2Q3, and P3Q4. Note that for close number of degrees of freedom (DoFs), the DG results are on coarser grids. For the lift, drag, pressure drag, and viscous drag all of the codes are approaching the same asymptotic values. HOMA shows a very close agreement with SFE at P1Q1 and the P2Q2 results are nearly mesh resolved even for the coarsest grid. The DG3D P1Q2 structured grid results are slightly better than the HOMA P1Q1 results; this can be attributed to both the grid type and the lack of high-order curving in the HOMA results. An exception is the coarsest DG3D P1Q2 structured grid which results in a negative viscous drag and therefor

also a negative total drag. This case has been converged to machine precision. Inspection of this case revealed that the negative value is due to the weak implementation of the no-slip boundary condition. For DG3D, the viscous forces are calculated based on the interior gradients and jump values at the solid boundaries. In this case, the jump values result in negative viscous forces. Although with mesh refinement, this problem is resolved, it is important to be mindful of such issues when running the discontinuous methods on coarse grids. Overall, the high-order results ($P > 1$) are showing more accurate than their lower order counterparts per degree of freedom. HOMA P2Q2 case requires the least number DoFs to reach the drag coefficients within two counts. The DG3D P1Q1 results on the tetrahedral grids are worse than the finite-volume and all the other finite-element results. This is a well-known problem which is remedied by using super-parametric elements. However, it is worth noting that this problem does not occur for the iso-parametric continuous finite-element discretizations and thus they have an advantage over discontinuous methods when using straight edged meshes at a polynomial degree of P1. For predicting the maximum eddy viscosity, both continuous finite-element solvers (SFE and HOMA) show less sensitivity to the mesh resolution. The FV and DG solvers require more resolution to reach the asymptotic value predicted by the SUPG solvers.

Figure 4 shows the grid convergence plots of the aerodynamic forces and maximum eddy viscosity for 19^o angle of attack. In this figure, the FUN3D FV results are shown on the tetrahedral grids. For the SFE, P1Q1 results are shown on the tetrahedral as well as hexahedral/prismatic grids. For the HOMA, P1Q1 and P2Q2 are shown for the tetrahedral grids, and P1Q1 solutions for the hexahedral/prismatic grids. For the DG3D, P1Q2 and P2Q3 results are shown for the structured (hex/prism) grids. For the force results, all the finite-element solutions converge to the same asymptotic values, however, this is not the case for the finite-volume solutions, especially for the lift coefficient. Compared to the results of the 5^o angle of attack, the advantages of the finite-element methods are less noticeable here; this could be attributed to the flow circulation and lack of mesh resolution in the upper wake region. HOMA shows slightly more accurate results compared to the SFE, and like SFE the hexahedral/prismatic grids give better solutions compared to the tetrahedral grids. For the viscous drag it appears that the HOMA results on hexahedral/prismatic grids are more accurate than those of the DG3D, but for the remaining components it is not clear which method is more accurate. The high-order finite-element results are more accurate than the lower-order ones per degree of freedom but the difference is not as drastic as the results of the 5^o angle of attack. Again, the maximum eddy viscosity is resolved more accurate by the SUPG solvers compared to the DG3D, while the FUN3D finite-volume discretization is still not mesh converged.

E. Linear and Nonlinear Convergence

In this subsection, the linear and nonlinear convergence behavior of the utilized finite-element solvers is investigated. Figures 5 and 6 demonstrate the operation of the PTC algorithm during the nonlinear solution for the case of 5^o angle of attack. These figures plot the total steady-state residual (in black), the CFL number (in red), the number of used Krylov vectors (in blue), and the maximum of the eddy viscosity (in green). The growth of the eddy viscosity shows the progress of the turbulence model equation, which has a key role in the convergence of the coupled system.

Figure 5 shows the convergence history of the HOMA solver on the tetrahedral grids 2-4 for two starting CFL numbers of 1 and 1000. Starting from a low CFL number (e.g. 1) is a common practice in using the PTC algorithm. Figures 5a, 5c, and 5e show that this practice may result in a severe mesh dependency of the solution algorithm as the finer grids take notably more non-linear iterations compared to coarser grids. For the finer grids, the non-linear residual is flat lined in the beginning while the eddy viscosity is slowly growing. Once a sufficient eddy viscosity develops, the CFL number begins to increase rapidly which at the same time makes the system of equations stiffer and increases the number of Krylov vectors needed to converge each

linear system. Figures 5b, 5d, and 5f show that by starting from a relatively high initial CFL = 1000, much of that startup phase can be skipped and all grids are solved in approximately 40 non-linear iterations. For grids 3 and 4, P2Q2 simulations are initialized using the previous P1Q1 solution which lead to rapid convergence. Even though with the CFL=1000 showing mesh independent nonlinear convergence, there is still a mesh dependency for the linear solver as seen in Figs. 5d and 5f, especially for P2Q2 simulations. This is due to the use a non-optimal preconditioner, which in this case is the implicit line method. This issue might be alleviated through the application of a linear multigrid method, which is reserved as a future work for the development of the utilized solvers. Also, further investigations are required to understand why the PTC algorithm might get stuck at low CFL numbers.

Figure 6 shows the convergence history of the DG3D solver on the structured grids 3-5 for initial CFL = 1000. It is difficult to summarize the DG3D results shown in this figure due to the large variations in each run. Solutions on grids 3 and 4 converge in fewer nonlinear steps compared to grid 5, and convergence history of grid 4 is comparable to the HOMA runs. Grid 5 is extremely coarse and that may be the cause of non-linear solver issues for the P1Q2 run. For this grid, when a P2Q3 run was initialized with the previous P1Q2 run it would not converge with the same settings, however P3Q4 did converge which is why it is shown in the figure. This issue was not observed in our previous study on the case of 0^o angle of attack [25]. This could be due to how the grids were generated. In that study, the coarser grids used less number of cells in each direction, but the thickness of the first cell in the boundary was maintained across all the grids. In the current study, only the finest grid maintains a y^+ of 0.5, and each coarser grid is nested inside the finer grid. Although these grids are expected to serve for a classical mesh resolution study, the lack of resolution near the boundary layer can disrupt the non-linear convergence path. This is in contract to the HOMA solver which appears to be less sensitive to the coarser grids.

F. Memory Considerations

In our previous work on the case of 0^o angle of attack [25], simulations using DG3D maxed out with a P4Q5 discretization. However, in this study P4Q5 simulations were unsuccessful due to memory constraints. This is due to the use of the Cheyenne supercomputer for this study whereas the Yellowstone supercomputer was used in the previous study. Although Cheyenne is a newer and faster machine it has less memory per core than Yellowstone did. The DG3D simulations presented in this work are partitioned based on lines and even going to the extreme of one cell-based line per core, a P4Q5 run was not achievable. If high-order methods are to be feasible on the next generation of computer architectures, memory limitations must be considered in development of the strong solvers required for these methods. This calls for development of low memory and optimal preconditioning and nonlinear solution techniques based on multilevel/multigrid methods.

V. Transonic Turbulent Flow over ONERA M6 Wing

The second configuration investigated in this paper is the ONERA M6 (OM6) wing. This configuration is widely used for CFD verification and validation exercises due to its simple geometry and availability of the experimental data. Similar to the hemisphere-cylinder configuration, the TMR website has provided grid generation and grid coarsening tools that provide the ability to generate various families of nested grids for mesh convergence studies. In addition, this website provides experimental data for two transonic flows at angles of attack of 3.06^o and 6.06^o. However, the reference numerical solutions have been provided only for the case of 3.06^o. In this paper, we run the mentioned finite-element solvers on both angles of attack, and attempt to provide insight into why the case of 6.06^o is difficult to solve.

A. Problem Description

The OM6 wing is a swept, semi-span wing based on a symmetric airfoil with no twist. The only modification to the original geometry of the wing is the use of a sharp trailing edge. Figure 7 shows the computational domain, boundary conditions, and the details of the geometry. The geometry is scaled such that the chord has a unit length and the spherical outer boundary has been placed at a distance of 100 units away from the wing. For this test case, the free-stream Mach number is 0.84, the Reynolds number based on the root chord is 14.6 million, and angles of attack are 3.06 and 6.06 degrees. The reference temperature and Prandtl numbers are the same as the hemisphere cylinder case. Also, the far-field, symmetry, and no-slip boundary conditions are applied in the same manner as the hemisphere cylinder case.

For shock capturing, artificial viscosity is added to the governing equations in order to stabilize the solution near the shock waves. The DG3D [41] solver uses a PDE-based artificial viscosity formulation [32, 33]. The HOMA solver's shock capturing term is similar to that of the SFE [9] with the difference that the shock sensor is calculated based on the Ref. [43].

B. Computational Grids

The computational grids for this test case are generated using the grid generator and grid coarsening codes provided by the TMR website. The grids for the OM6 are topologically the same as the hemisphere cylinder grids described in the previous section. The finest grid has 384 nodes along the wing section, 192 nodes in the span-wise direction (excluding the wing tip), and 704 nodes in the normal direction to the wing surface. For this mesh, the spacing normal to the wall is such that a $y^+ = 0.5$ is targeted. However, like the hemisphere-cylinder case, the coarsening the algorithm does not maintain this value for the coarser grids. Unfortunately, unlike the hemisphere-cylinder case, the mesh curving approach using the removed vertices form the finer grids results in elements with negative Jacobians in the geometrical mapping, especially near the trailing edge of the wing tip. This might be due to large jumps in the element sizes at this region (see Fig. 7b). Thus, both finite-element solvers are utilized on Q1 grids. HOMA utilizes the tetrahedral grids from the second family, and the DG3D utilizes structured (hex/prism) grids from family 5. Tables 3 and 4 show the statistics of the utilized grids for both solvers in this study. In addition to the TMR grids, we generated two custom tetrahedral grids using the Pointwise software. Both custom grids have the same surface and boundary layer meshes. However, custom grid 2 has more refinement in the wake region. The motivation behind the generation of these grids is explained in Section V.D.

C. Wall Distance

The wall distance for both finite-element solvers is based on a brute force search over the surface elements. For the DG solver, quadrilateral faces are converted to two triangles and wall distance is measured from those surface triangulations to every quadrature point in the cells. For the SUPG solver the wall distance is calculated at every node and projected using linear interpolation to the interior quadrature points.

Table 3. Statistics of the utilized OM6 grids for the stabilized finite-element solver

Grids	Family 2 (Tet)			Custom (Tet)	
	Elements	P1 DOFs	P2 DOFs	Elements	P1 DOFs
2	45,416,448	7,625,153	-	10,080,581	1,721,878
3	5,677,056	960,225	-	15,979,900	2,711,199
4	709,632	121,841	960,225	-	-
5	88,704	15,705	121,841	-	-

Table 4. Statistics of the utilized OM6 grids for the discontinuous Galerkin solver

Grids	Family 5 (Hex/Prism)		
	Elements	P1 DOFs	P2 DOFs
3	1,081,344	8,616,960	-
4	135,168	1,072,896	-
5	16,896	133,056	446,688

D. Results

Figure 9 shows the grid convergence of the aerodynamics forces and the maximum eddy viscosity for different flow solvers at the angle of attack of 3.06°. FUN3D FV results are shown for the prismatic grids, SFE and HOMA P1Q1 solutions are shown for the tetrahedral grids, and DG3D P1Q1 results are shown for the structured (hex/prism) grids. The drag results appear to be reaching an asymptotic value but the lift and maximum eddy viscosity seem to be a few grids away from the asymptote. HOMA P1Q1 results for all subfigures are converging most rapidly out of all of the solvers. This solver is slightly outperforming SFE results but this might be attributed to the use of the weak boundary conditions by HOMA, and strong boundary conditions by SFE. DG3D P1Q1 and HOMA P2Q1 results are not very accurate. This is similar to what we have seen before for the DG discretization which requires a curved mesh with at least $Q = P + 1$ to deliver the nominal order of accuracy. HOMA P2Q1 solutions demonstrate that the SUPG discretization is also sensitive to the mesh curving and needs at least a mapping polynomial degree of $Q = P$. It is difficult to say which solver is correctly predicting the maximum eddy viscosity due to the scatter in the Fig. 9e. However, HOMA appears to be converging while FUN3D is changing more rapidly with mesh refinement.

Figure 10 shows the convergence history of the HOMA solver on three tetrahedral grids (3,4, and 5) and two angles of attack (3.06° and 6.06°). The DG3D convergence history is not shown due to the lack of mesh curving (running without proper mesh curving is proved to be difficult for the non-linear solver and it was hard to draw any conclusions). Similar to the hemisphere-cylinder case, the PTC non-linear solver handles these cases well. Although not shown, HOMA converges on the tetrahedral grid 2 at angle 3.06°, but not at angle 6.06°. An interesting point in Fig. 10 about the solutions of angle 6.06° is that by grid refinement, the maximum eddy viscosity increases rapidly. This can also be seen in Fig. 11, which summarize the grid convergence results for angle 6.06°. Based on this figure, it is hard to make any predictions on forces or maximum eddy viscosity due to the lack of consistency between the finite-element solvers. Also, no reference solution is given by the TMR website for this case. These results are shown to demonstrate that solutions are possible and this could be useful for future studies. However, further investigations are required to understand the reason behind the growth of the eddy viscosity with mesh refinement. It is difficult to compare accuracy of the two finite-element solvers in this work, however, the DG3D maximum eddy viscosity values are very large and significantly different than HOMA. Large values of eddy viscosity can indicate the presence of a large recirculation region in the solution. The authors initially suspected the topology of the TMR grids were the main cause of the issue, but after running on the custom grids we believe that it is the particular flow conditions that are causing the problems.

Figure 12 shows the convergence history of the HOMA solver on two custom tetrahedral grids and two angles of attack (3.06° and 6.06°). As seen, for angle 3.06°, both grids take about 40 nonlinear iterations to converge. However, for angle 6.06°, custom grid 1 takes over 130 non-linear iterations, and custom grid 2 does not converge even after 400 iterations. Figure 13 shows the flow visualization on custom grid 1 at angle 3.06° with contours of pressure in Fig. 13a and contours of eddy viscosity and streamlines in Fig. 13b. The shock

on the upper surface of the wing is sharp and well resolved and the streamlines show the tip vortex well. Figure 14 shows flow visualization for the two custom grids at angle of attack 6.06°. Figure 14a and 14b show contours of pressure at the wing tip for both custom grids. The solution at the tip is drastically different between the two grids. Even though the solution is not converged in 15b the differences are large given that the mesh is very similar in this region. As mentioned earlier these grids have the same surface and boundary layers meshes, and the only difference is that the second mesh has more refinement in the wake region. Figures 14c and 14d show the differences in the tip vortex with streamline visualization. This gives further evidence to how sensitive this case is to the grids and to resolution in the wake region. The custom grids were used here to help diagnose the issues found with the angle 6.06° and give us more insight about the inconsistent results shown for this angle of attack.

VI. Conclusions

This work investigates the accuracy and performance of a SUPG and a DG finite element method on 3D turbulent flows. Simulations of TMR problems on hemisphere cylinder and ONERA M6 wings were carried out and integrated forces and maximum eddy viscosity were compared to the NASA FUN3D flow solver. The hemisphere cylinder at angle of attack of 5° approached asymptotic values for integrated forces for all discretizations. The finite element solvers had more accurate solutions per degree of freedom compared to the FUN3D finite-volume solver. The most accurate discretization per degree of freedom within a reasonable tolerance (2 counts) is obtained using a P2Q2 SUPG discretization. The non-linear convergence history was studied for hemisphere cylinder at alpha 5. The SUPG solver showed a very consistent non-linear convergence for all grids. Mesh dependence still shows up in the linear solver with an increase in the number of Krylov vectors needed for finer meshes. Also reported are some non-linear convergence histories for the DG solver which shows similar convergence to SUPG solver for some cases but has more difficulty on others especially on extremely coarse meshes. The hemisphere cylinder at angle of attack of 19° also showed reasonable results. It is not clear if the finite-volume solver of FUN3D is quite mesh resolved yet, whereas the finite-element solvers converge to similar solutions. Even though the finite element solvers are more accurate than finite-volume, in this case it is still not as drastic as in the alpha 5 case. At this angle of attack, some of the grids used may not have enough resolution needed in the wake region.

The ONERA M6 wing case at alpha 3.06 is more difficult than the hemisphere cylinder but solutions are found for all of the discretizations. ONERA M6 at alpha 3.06 gives accurate solutions for the SUPG solver and consistent convergence history for all grids. The DG solver does not give accurate results but this is due to the use of straight edged tetrahedral meshes. Similar solution degradation is seen when attempting to use the SUPG solver with a polynomial degree of P2Q1. There are no TMR results for alpha 6.06 ONERA M6 but attempts were made to simulate with both finite-element solvers. For this angle of attack, there are no signs of convergence of integrated forces. Finer meshes appear to be harder on the non-linear solver than coarse meshes. Two custom unstructured grids were created to further investigate this issue. Solutions are found on some grids and not others and this appears to be an issue with the flow itself and not with the TMR provided grids.

Acknowledgments

This research was sponsored by NASA's Transformational Tools and Technologies (TTT) Project of the Transformative Aeronautics Concepts Program under the Aeronautics Research Mission Directorate.

References

[1] C. Rumsey. *Turbulence Modeling Resource Website*. Available: http://turbmodels.larc.nasa.gov

[2] K. S. Abdol-Hamid, J.-R. Carlson, and C. L. Rumsey, "Verification and Validation of the k-kL Turbulence Model in FUN3D and CFL3D Codes," AIAA Paper 2016-3941, 2016.

[3] B. Diskin, J. L. Thomas, C. L. Rumsey, and A. Schwöppe, "Grid-Convergence of Reynolds-Averaged Navier–Stokes Solutions for Benchmark Flows in Two Dimensions," *AIAA Journal,* 2016.

[4] M. J. Pandya, B. Diskin, J. L. Thomas, and N. T. Frink, "Improved Convergence and Robustness of USM3D Solutions on Mixed-Element Grids," *AIAA Journal,* 2016.

[5] M. J. Pandya, B. Diskin, J. L. Thomas, and N. T. Frink, "Assessment of USM3D Hierarchical Adaptive Nonlinear Method Preconditioners for Three-Dimensional Cases," *AIAA Journal,* pp. 1-16, 2017.

[6] E. J. Nielsen and W. K. Anderson, "Recent improvements in aerodynamic design optimization on unstructured meshes," *AIAA Journal,* vol. 40, pp. 1155-1163, 2002.

[7] W. K. Anderson, R. D. Rausch, and D. L. Bonhaus, "Implicit/multigrid algorithms for incompressible turbulent flows on unstructured grids," *Journal of Computational Physics,* vol. 128, pp. 391-408, 1996.

[8] W. K. Anderson and D. L. Bonhaus, "An implicit upwind algorithm for computing turbulent flows on unstructured grids," *Computers & Fluids,* vol. 23, pp. 1-21, 1994.

[9] W. K. Anderson, J. C. Newman, and S. L. Karman, "Stabilized Finite Elements in FUN3D," *Journal of Aircraft,* pp. 1-19, 2017.

[10] D. A. Brown, H. Buckley, M. Osusky, and D. W. Zingg, "Performance of a Newton-Krylov-Schur Algorithm for the Numerical Solution of the Steady Reynolds-Averaged Navier-Stokes Equations (Invited)," AIAA Paper 2015-1744, 2015.

[11] V. Gleize, A. Dumont, J. Mayeur, and D. Destarac, "RANS simulations on TMR test cases and M6 wing with the Onera elsA flow solver (Invited)," AIAA Paper 2015-1745, 2015.

[12] B. Diskin, J. Thomas, C. L. Rumsey, and A. Schwoeppe, "Grid Convergence for Turbulent Flows (Invited)," AIAA Paper 2015-1746, 2015.

[13] M. J. Brazell and D. J. Mavriplis, "High-Order Discontinuous Galerkin Mesh Resolved Turbulent Flow Simulations of a NACA 0012 Airfoil (Invited)," AIAA Paper 2015-1529, 2015.

[14] Y. Hu, C. Wagner, S. Allmaras, M. Galbraith, and D. L. Darmofal, "Application of a Higher-order Adaptive Method to RANS Test Cases (Invited)," AIAA Paper 2015-1530, 2015.

[15] M. J. Pandya, B. Diskin, J. Thomas, and N. T. Frink, "Improved Convergence and Robustness of USM3D Solutions on Mixed Element Grids (Invited)," AIAA Paper 2015-1747, 2015.

[16] W. K. Anderson, B. R. Ahrabi, and J. C. Newman III, "Finite-element solutions for turbulent flow over the NACA 0012 airfoil (Invited)," presented at the 53rd AIAA Aerospace Sciences Meeting, AIAA Paper 2015-1531, 2015.

[17] M. Ceze and K. Fidkowski, "High-Order Output-Based Adaptive Simulations of Turbulent Flow in Two Dimensions (Invited)," AIAA Paper 2015-1532, 2015.

[18] W. K. Anderson, B. R. Ahrabi, and J. C. Newman, "Finite Element Solutions for Turbulent Flow over the NACA 0012 Airfoil," *AIAA Journal,* vol. 54, No. 9, pp. 2688-2704, Sept 2016.

[19] M. J. Brazell, D. J. Mavriplis, and Z. Yang, "Mesh-Resolved Airfoil Simulations Using Finite Volume and Discontinuous Galerkin Solvers," *AIAA Journal,* vol. 54, pp. 2659-2670, 2016.

[20] M. A. Ceze and K. J. Fidkowski, "High-Order Output-Based Adaptive Simulations of Turbulent Flow in Two Dimensions," *AIAA Journal,* vol. 54, pp. 2611-2625, 2016.

[21] M. J. Pandya, B. Diskin, J. L. Thomas, and N. T. Frink, "Improved Convergence and Robustness of USM3D Solutions on Mixed-Element Grids," *AIAA Journal,* vol. 54, pp. 2589-2610, 2016.

[22] Y. Hu, C. Wagner, S. R. Allmaras, M. C. Galbraith, and D. L. Darmofal, "Application of Higher-Order Adaptive Method to Reynolds-Averaged Navier–Stokes Test Cases," *AIAA Journal,* vol. 54, pp. 2626-2644, 2016.

[23] B. Diskin, J. Thomas, C. L. Rumsey, and M. J. Pandya, "Reference Solutions for Benchmark Three Dimensional Turbulent Flows," AIAA Paper 2016-0858, 2016.

[24] M. A. Park and W. K. Anderson, "Spatial Convergence of Three Dimensional Turbulent Flows," AIAA Paper 2016-0859, 2016.

[25] M. J. Brazell, B. R. Ahrabi, and D. J. Mavriplis, "Discontinuous Galerkin Turbulent Flow Simulations of NASA Turbulence Model Validation Cases and High Lift Prediction Workshop Test Case DLR-F11," AIAA Paper 2016-0861, 2016.

[26] K. Fidkowski and M. Ceze, "High-Order Output-Based Adaptive Simulations of Turbulent Flow in Three Dimensions (Invited)," AIAA Paper 2016-0862, 2016.

[27] J. T. Erwin and R. S. Glasby, "Application of HPCMP CREATE^{TM}-AV COFFE for Three-Dimensional Turbulent Flow Cases," vol. AIAA Paper 2016-1361, 2016.

[28] B. R. Ahrabi and D. J. Mavriplis, "Scalable Solution Strategies for Stabilized Finite-Element Flow Solvers on Unstructured Meshes," presented at the 55th AIAA Aerospace Sciences Meeting, AIAA Paper 2017-0517, Dallas, TX, January 2017.

[29] B. Reza Ahrabi and D. J. Mavriplis, "Scalable Solution Strategies for Stabilized Finite-Element Flow Solvers on Unstructured Meshes, Part II," presented at the 23rd AIAA Computational Fluid Dynamics Conference, AIAA Paper 2017-4275, Denver, Colorado, June 2017.

[30] C. T. Kelley and D. E. Keyes, "Convergence analysis of pseudo-transient continuation," *SIAM Journal on Numerical Analysis,* vol. 35, pp. 508-523, 1998.

[31] M. Ceze and K. J. Fidkowski, "Constrained pseudo-transient continuation," *International Journal for Numerical Methods in Engineering,* vol. 102, pp. 1683-1703, 2015.

[32] P.-O. Persson and J. Peraire, "An efficient low memory implicit DG algorithm for time dependent problems," presented at the 44th AIAA Aerospace Sciences Meeting and Exhibit, AIAA Paper 2006-0113, 2006.

[33] G. E. Barter and D. L. Darmofal, "Shock capturing with PDE-based artificial viscosity for DGFEM: Part I. Formulation," *Journal of Computational Physics,* vol. 229, pp. 1810-1827, 2010.

[34] S. R. Allmaras and F. T. Johnson, "Modifications and clarifications for the implementation of the Spalart-Allmaras turbulence model," in *Seventh International Conference on Computational Fluid Dynamics (ICCFD7)*, 2012, pp. 1-11.

[35] P. D. Lax, "Weak solutions of nonlinear hyperbolic equations and their numerical computation," *Communications on pure and applied mathematics,* vol. 7, pp. 159-193, 1954.

[36] P. L. Roe, "Approximate Riemann solvers, parameter vectors, and difference schemes," *Journal of computational physics,* vol. 43, pp. 357-372, 1981.

[37] M. Sun and K. Takayama, "An artificially upstream flux vector splitting scheme for the Euler equations," *Journal of Computational Physics,* vol. 189, pp. 305-329, 2003.

[38] R. Hartmann and P. Houston, "An optimal order interior penalty discontinuous Galerkin discretization of the compressible Navier–Stokes equations," *Journal of Computational Physics,* vol. 227, pp. 9670-9685, 2008.

[39] K. Shahbazi, D. J. Mavriplis, and N. K. Burgess, "Multigrid algorithms for high-order discontinuous Galerkin discretizations of the compressible Navier–Stokes equations," *Journal of Computational Physics,* vol. 228, pp. 7917-7940, 2009.

[40] Y. Saad, *Iterative Methods for Sparse Linear Systems*: Siam, 2003.

[41] M. J. Brazell and D. J. Mavriplis, "3D mixed element discontinuous Galerkin with shock capturing," AIAA Paper 2013-3064, 2013.

[42] M. J. Brazell, J. Sitaraman, and D. J. Mavriplis, "An overset mesh approach for 3D mixed element high-order discretizations," *Journal of Computational Physics,* vol. 322, pp. 33-51, 2016.

[43] Ryan S. Glasby, J. Taylor Erwin, Douglas L. Stefanski, Steve L. Karman, and W. K. Anderson, "Results from HPCMP CREATETM-AV COFFE for Tasks 1-3 for DPW6," in *6th AIAA CFD Drag Prediction Workshop, AIAA Aviation 2016, Washington, D.C., 16-17 June 2016.*

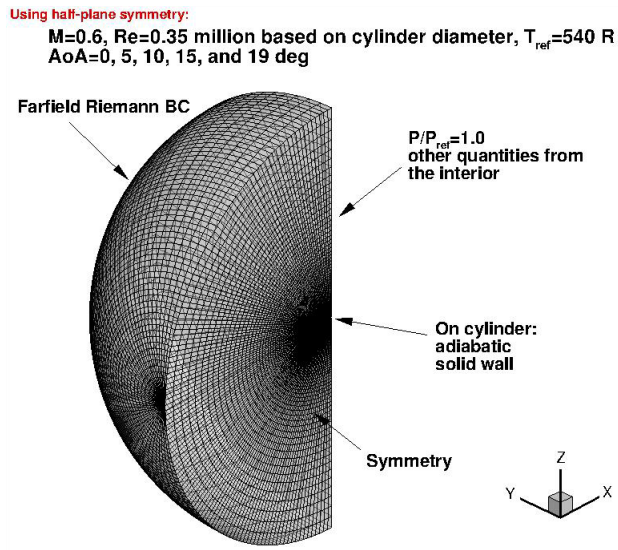

(a) Picture from the TMR website [1]

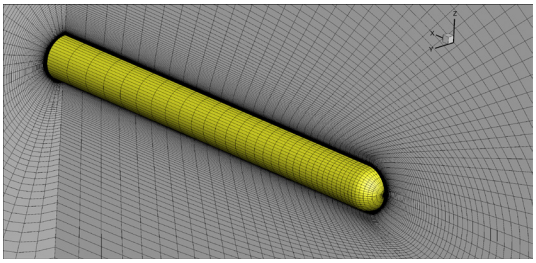

(b) Structured (hex/prism) grid 4

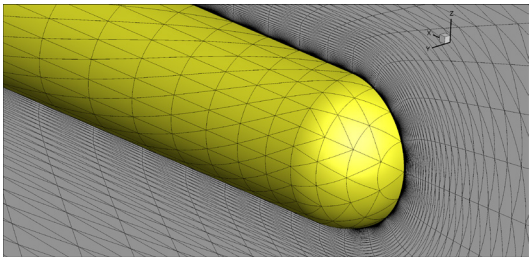

(c) Tetrahedral grid 5 (curved)

Figure 1. Computational domain, boundary conditions, and sample grids for the hemisphere-cylinder case.

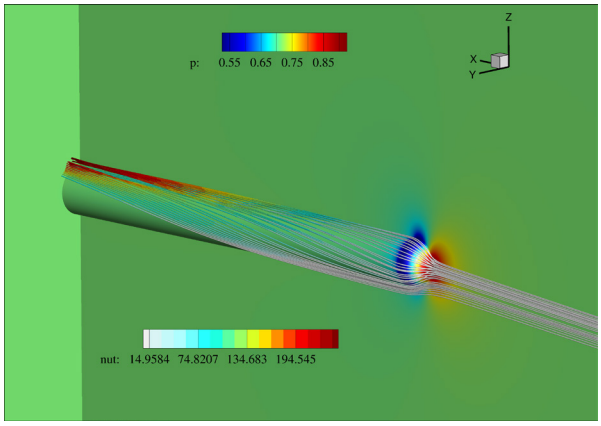

(a) Angle of attack of 5°

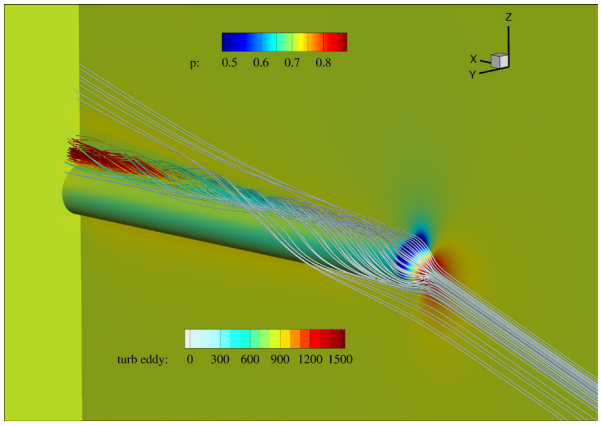

(b) Angle of attack of 19°

Figure 2. Flow visualization for hemisphere cylinder test case at two angles of attack (stream lines are colored by the eddy viscosity).

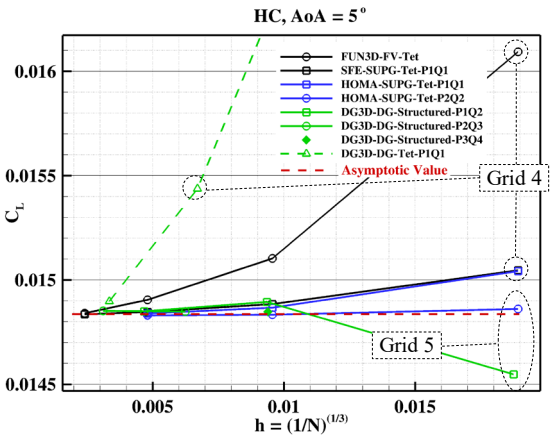

(a) Lift coefficient

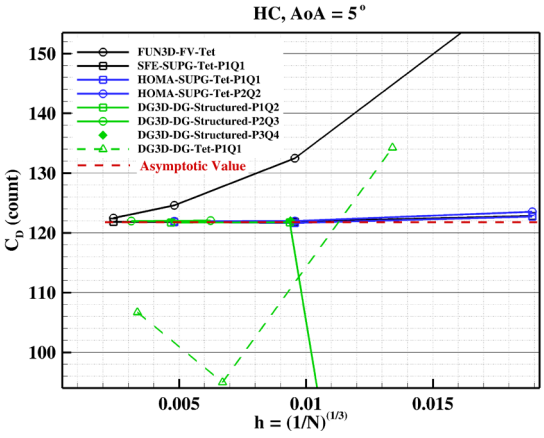

(b) Total drag coefficient

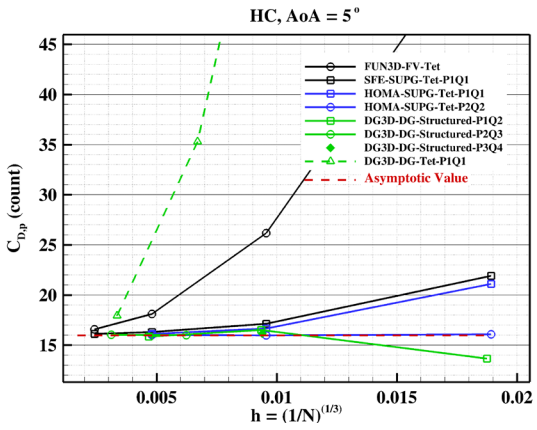

(c) Pressure drag coefficient

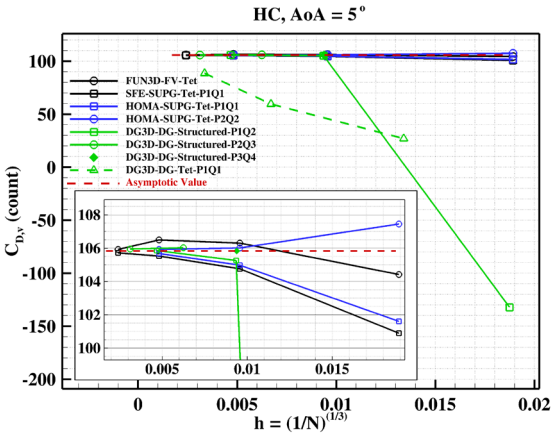

(d) Viscous drag coefficient

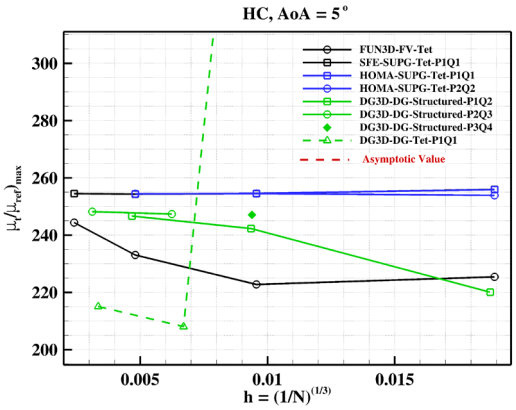

(e) Maximum eddy viscosity

Figure 3. Grid convergence of aerodynamic force coefficients and maximum eddy viscosity for the hemisphere test case at angle of attack of 5 degrees.

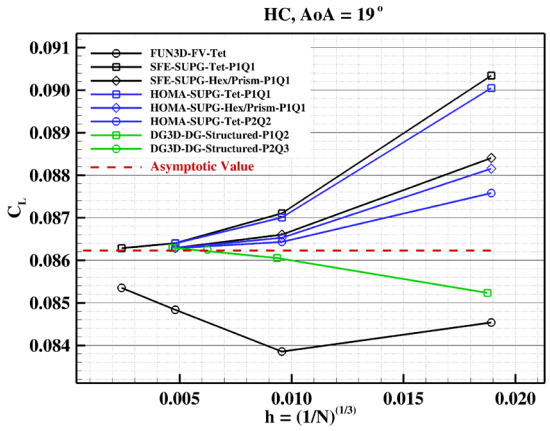

(a) Lift coefficient

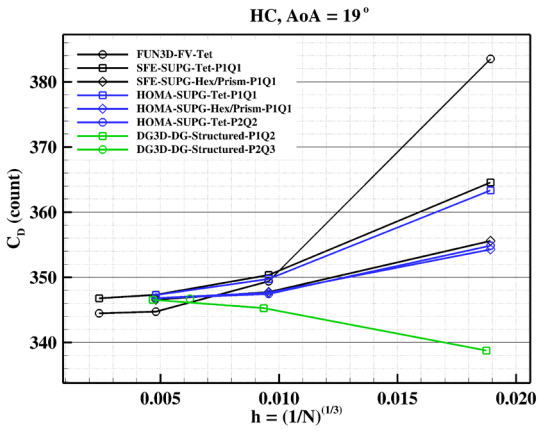

(b) Total drag coefficient

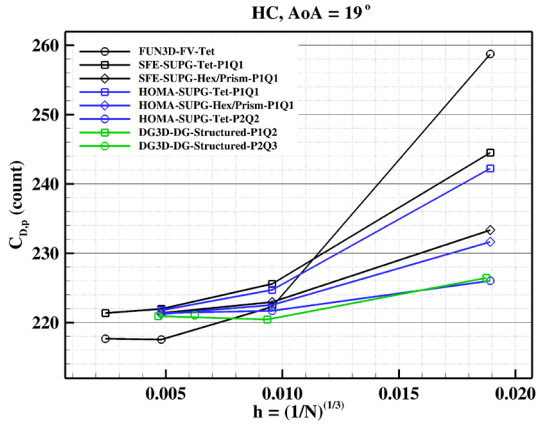

(c) Pressure drag coefficient

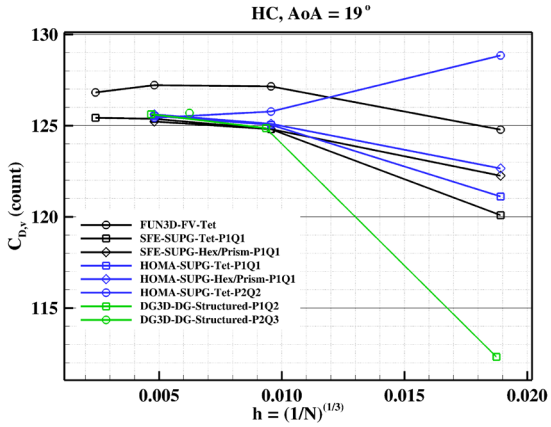

(d) Viscous drag coefficient

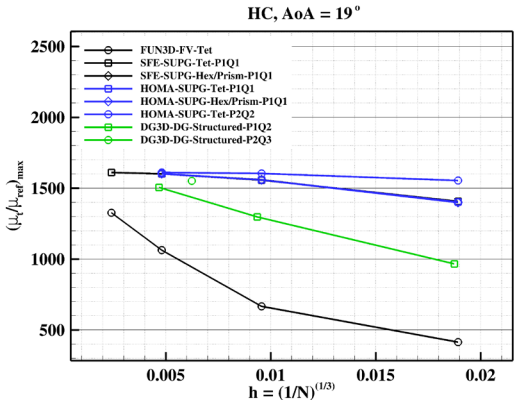

(e) Maximum eddy viscosity

Figure 4. Grid convergence of aerodynamic force coefficients and maximum eddy viscosity for the hemisphere-cylinder case at angle of attack of 19 degrees.

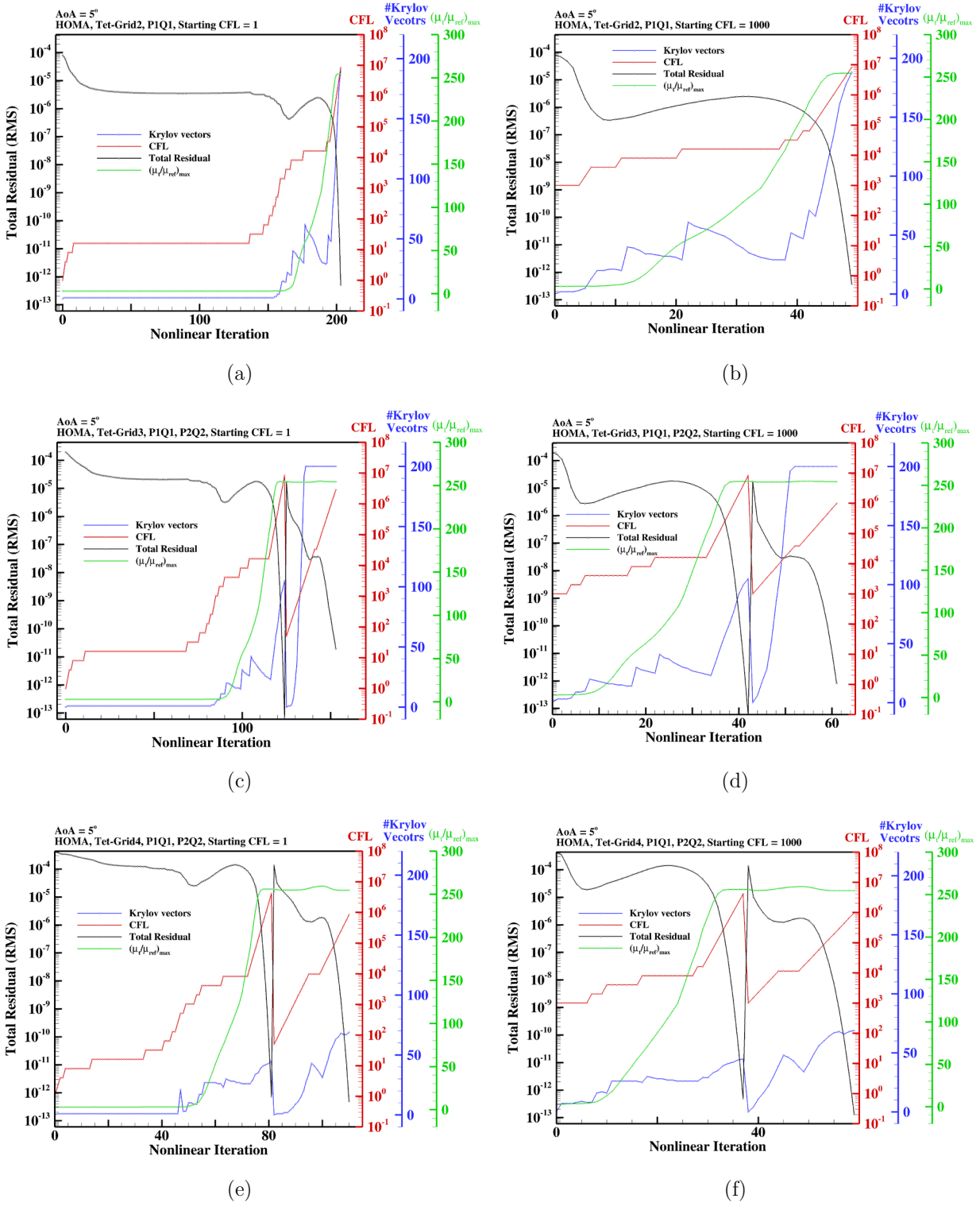

Figure 5. Operation of the PTC algorithm with different starting CFL values using the stabilized finite-element solver (HOMA) on tetrahedral grids for the hemisphere test case at angle of attack of 5 degrees. (a,b) P1Q1 solutions, (c-f) P1 and P2 solutions. P1 solutions are initialized by the free stream conditions, and P2 solutions are initialized by the converged P1 solutions.

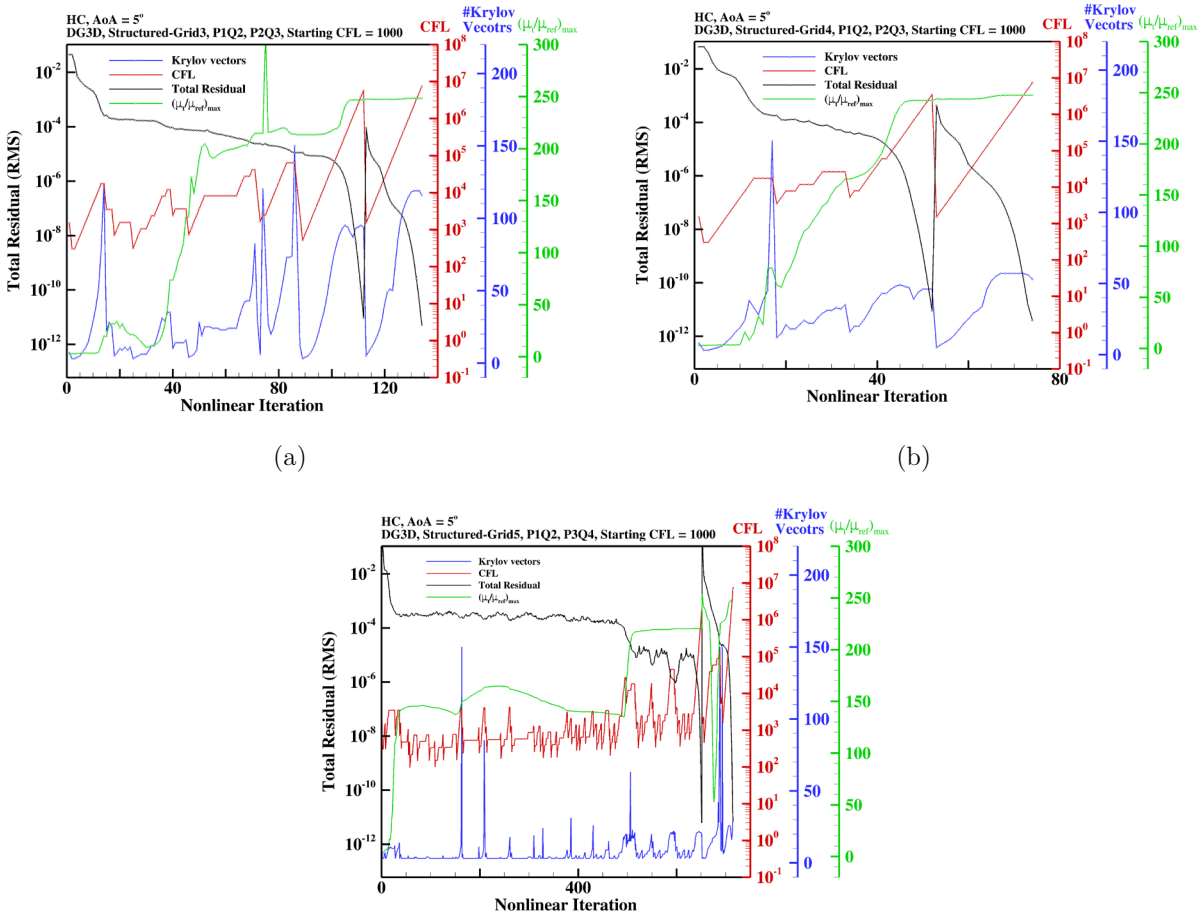

Figure 6. Operation of the PTC algorithm with starting CFL of 1000.0 using the discontinuous Galerkin finite-element solver (DG3D) on the structured grids for the hemisphere test case at angle of attack of 5 degrees. (a,b) P1 and P2 solutions, (c) P1 and P3 solution. P1 solutions are initialized by the free stream conditions, and P2, P3 solutions are initialized by the converged P1 solutions.

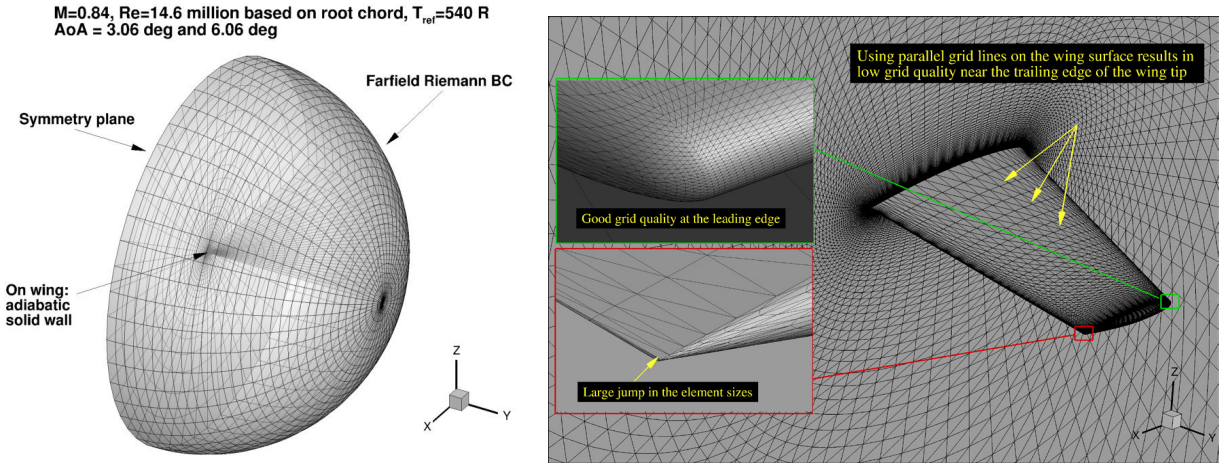

(a) Computational domain [1] (b) Grid 4 from family 2 (Tet)

Figure 7. Computational domain and a sample TMR grid for the ONEAR M6 wing.

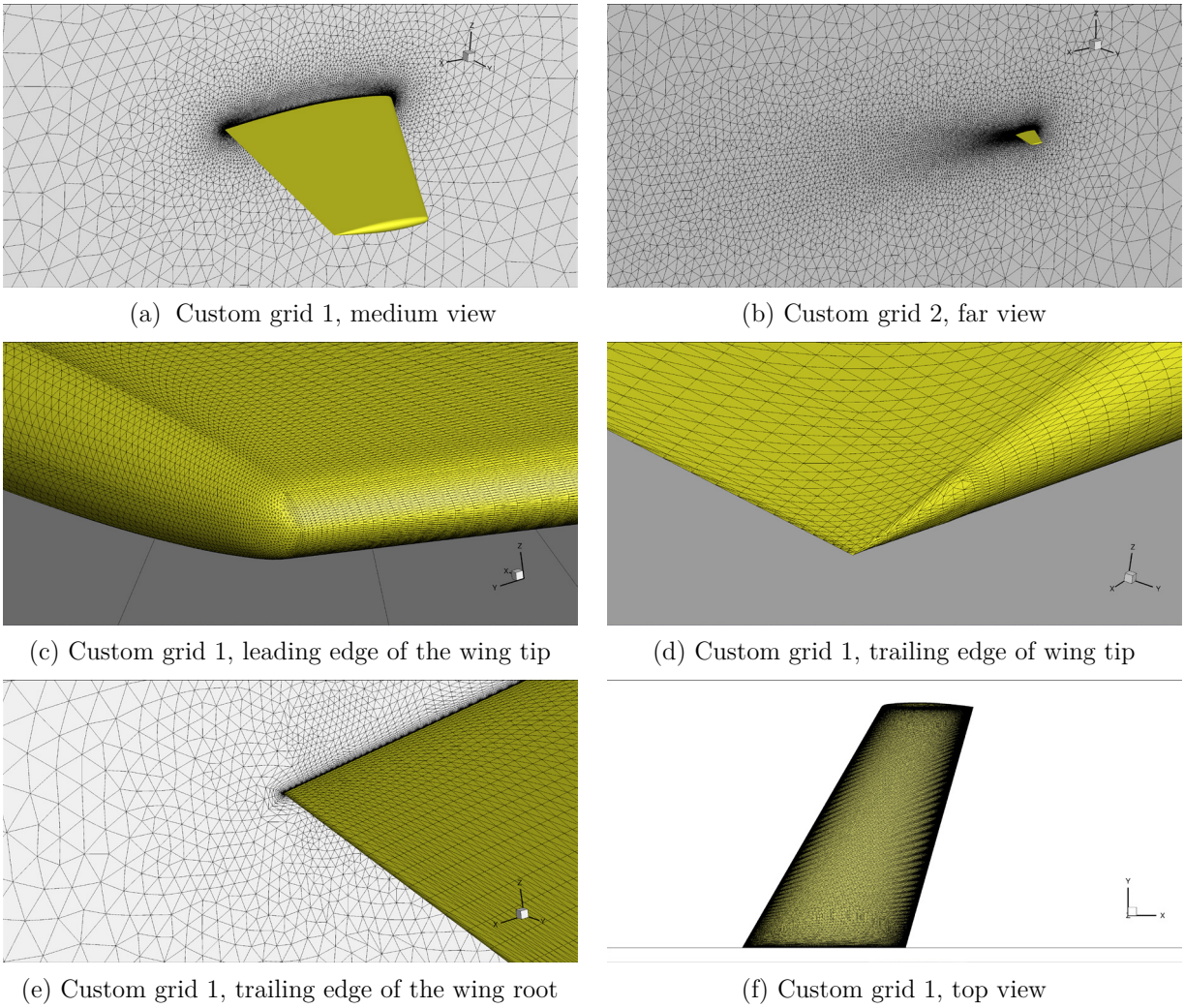

(a) Custom grid 1, medium view (b) Custom grid 2, far view

(c) Custom grid 1, leading edge of the wing tip (d) Custom grid 1, trailing edge of wing tip

(e) Custom grid 1, trailing edge of the wing root (f) Custom grid 1, top view

Figure 8. Custom grids 1 and 2 for the ONERA M6 wing. Both grids have the same surface and boundary layer mesh, but custom grid 2 has more refinement in the wake region.

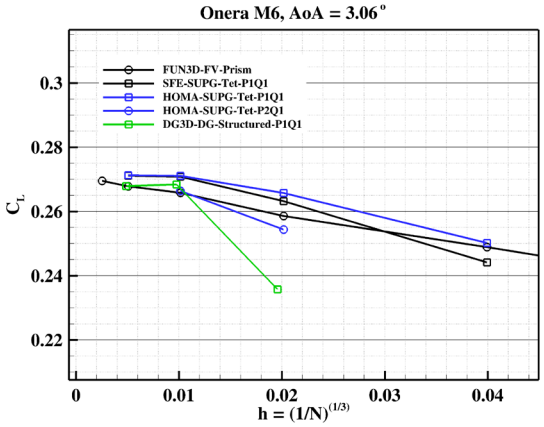

(a) Lift coefficient

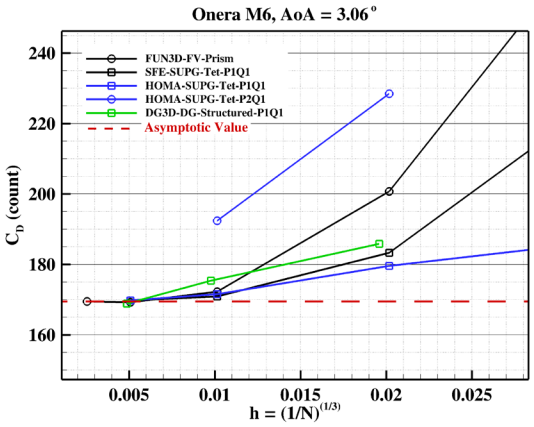

(b) Total drag coefficient

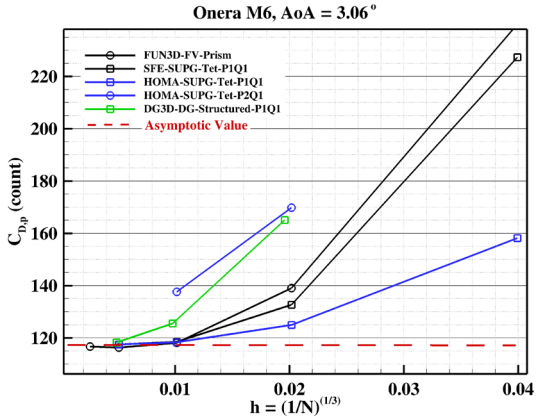

(c) Pressure drag coefficient

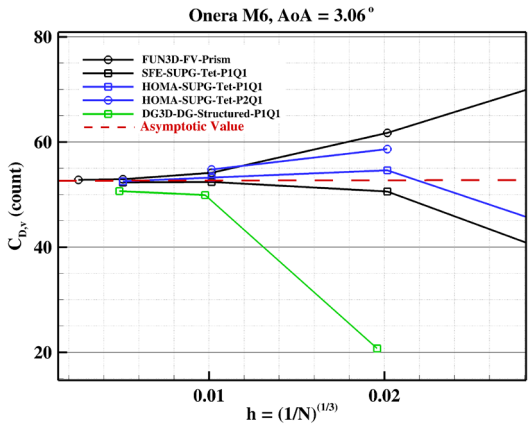

(d) Viscous drag coefficient

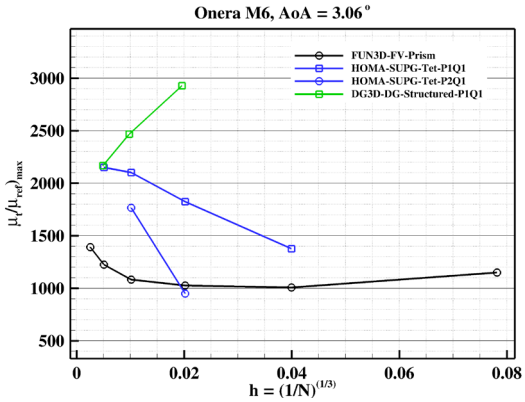

(e) Maximum eddy viscosity

Figure 9. Grid convergence of aerodynamic force coefficients and maximum eddy viscosity for the ONERA M6 test case at angle of attack of 3.06 degrees.

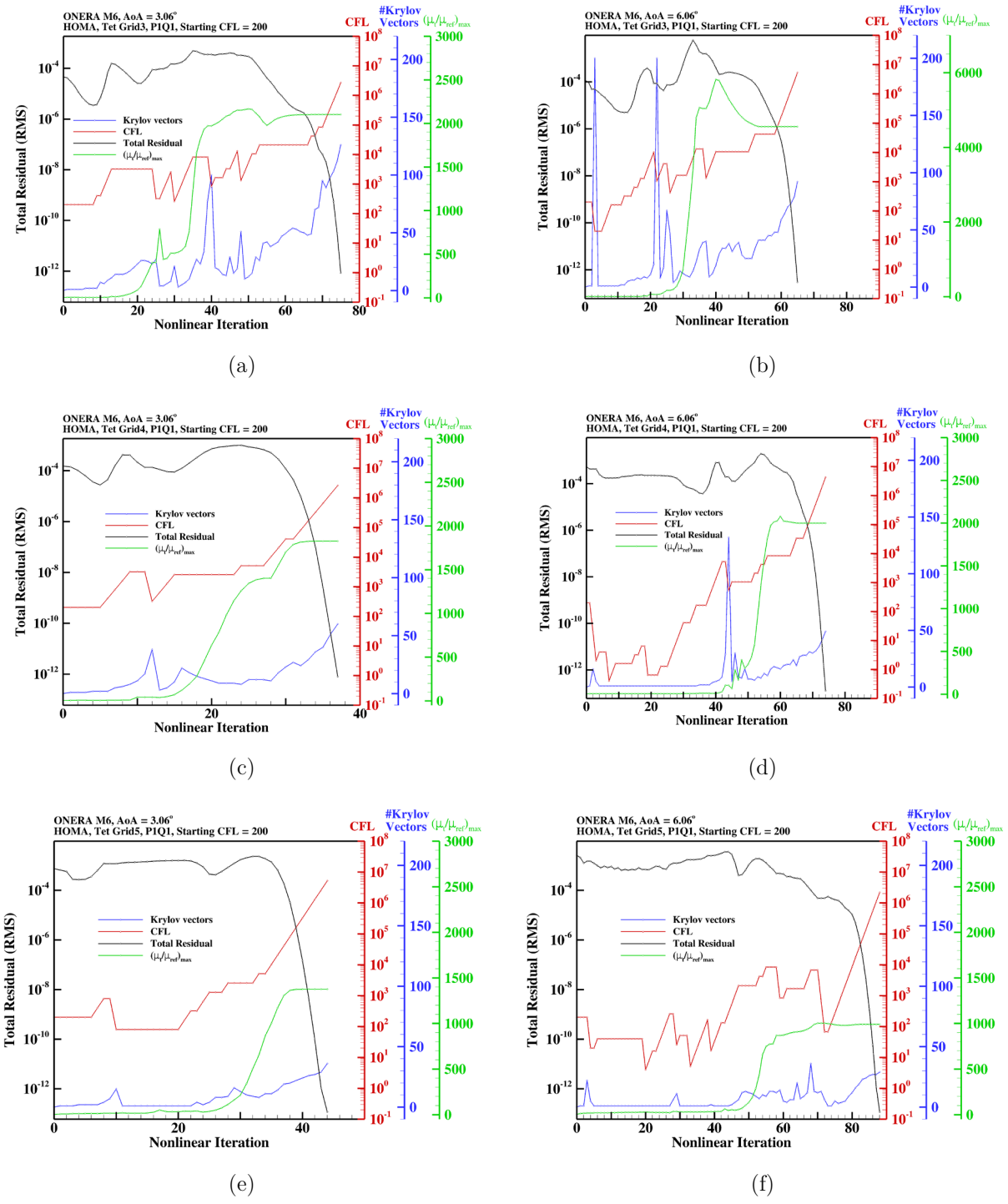

Figure 10. Convergence history of the stabilized finite-element solver (HOMA) for the ONERA M6 test case on the TMR tetrahedral grids at different angles of attack.

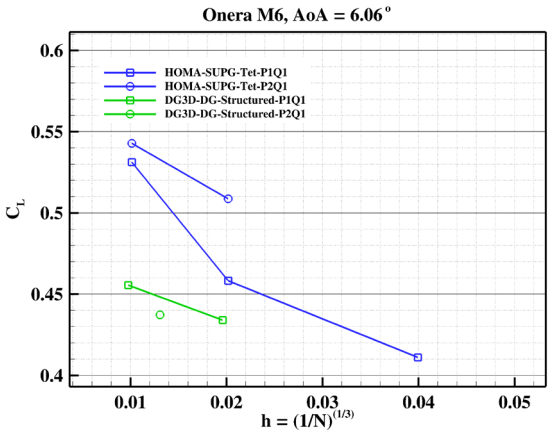

(a) Lift coefficient

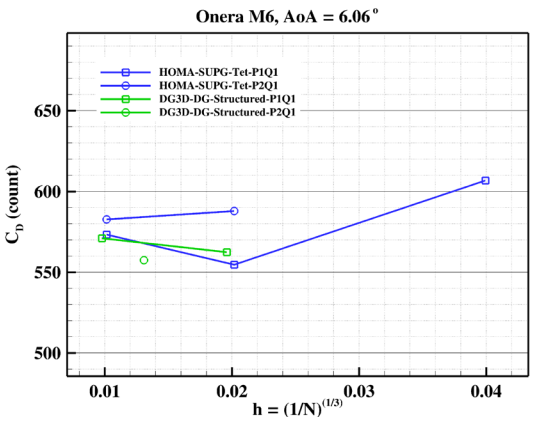

(b) Total drag coefficient

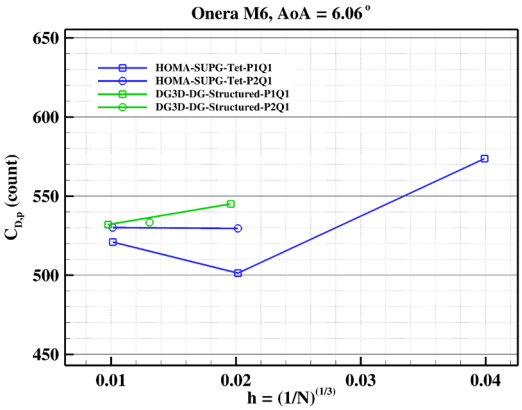

(c) Pressure drag coefficient

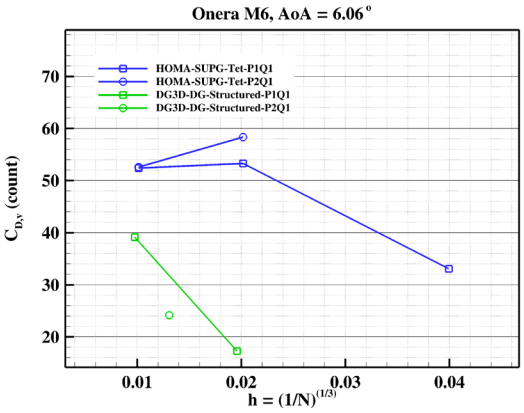

(d) Viscous drag coefficient

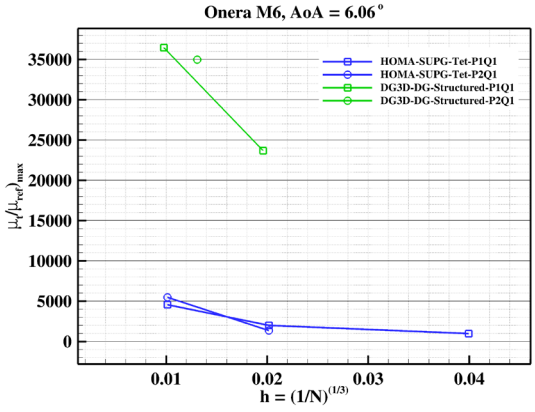

(e) Maximum eddy viscosity

Figure 11. Grid convergence of aerodynamic force coefficients and maximum eddy viscosity for the ONERA M6 test case at angle of attack of 6.06 degrees.

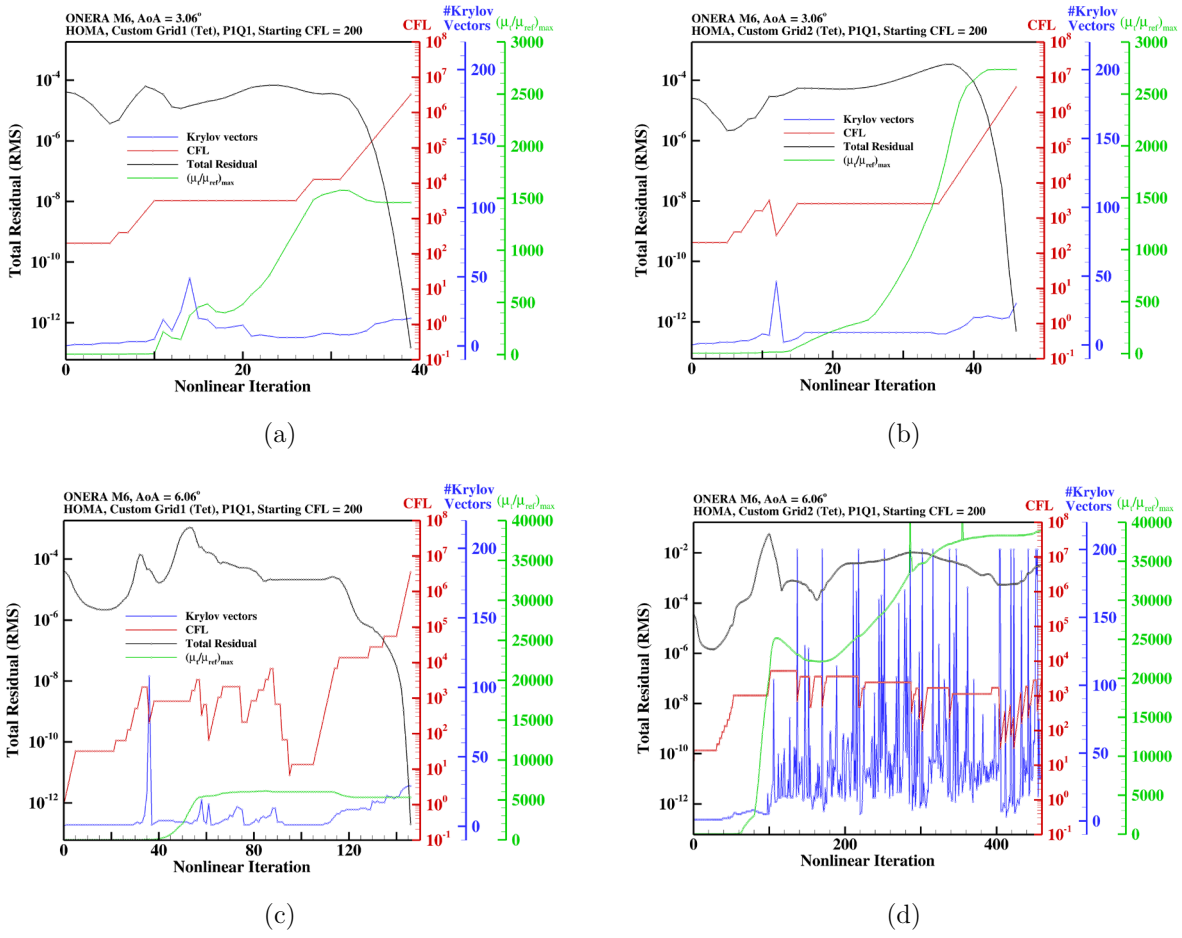

Figure 12. Convergence history of the stabilized finite-element solver (HOMA) for the ONERA M6 test case on the custom tetrahedral grids at different angles of attack.

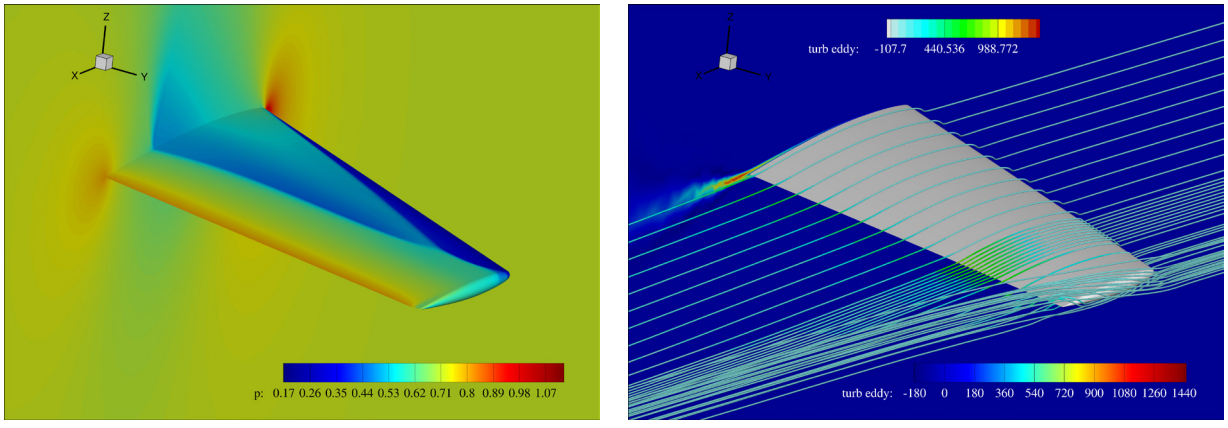

(a) Pressure

(b) Turbulent working variable

Figure 13. Flow visualization for the ONERA M6 wing at Mach number of 0.84, Reynolds number of 14.6 million, and angle of attack of 3.06° on the custom grid 1.

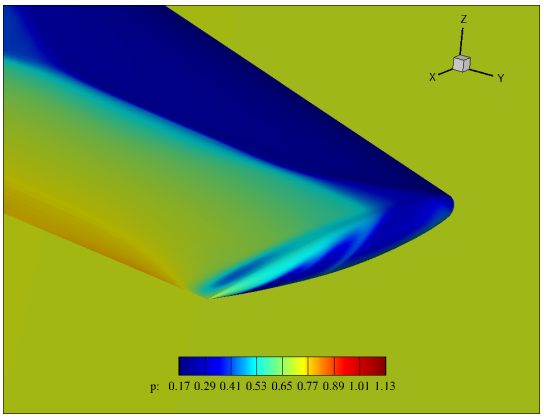

(a) Custom grid 1 (fully converged solution)

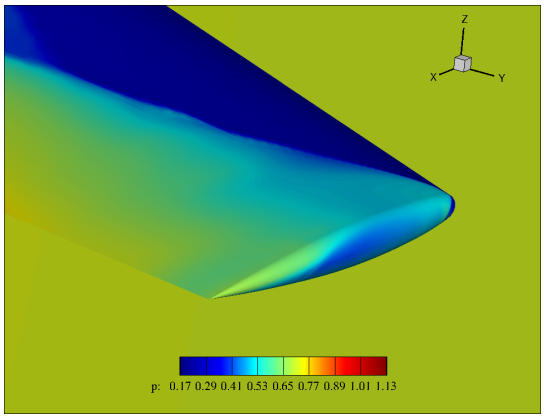

(b) Custom grid 2 (unconverged solution)

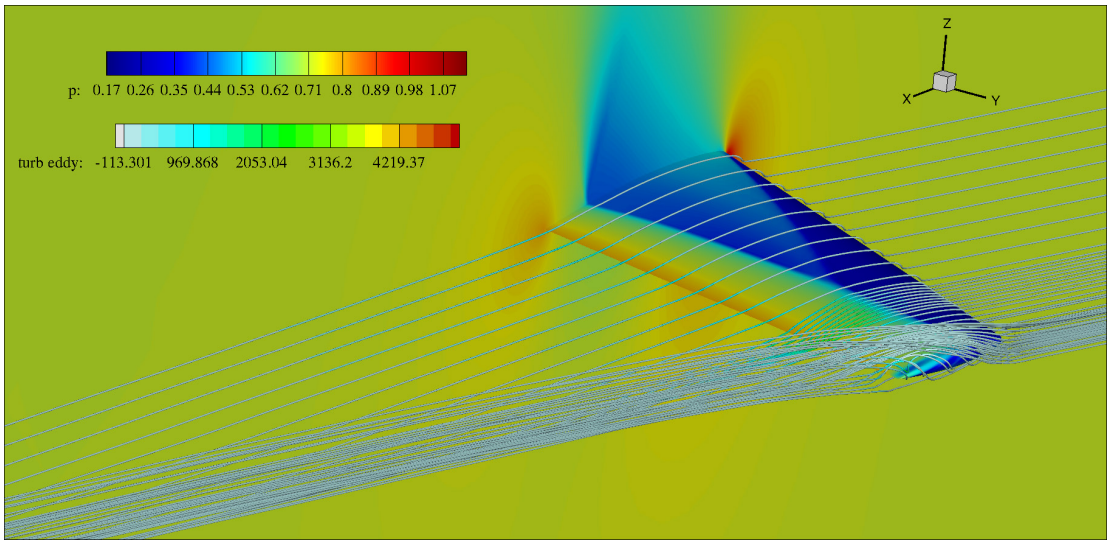

(c) Custom grid 1 (fully converged solution)

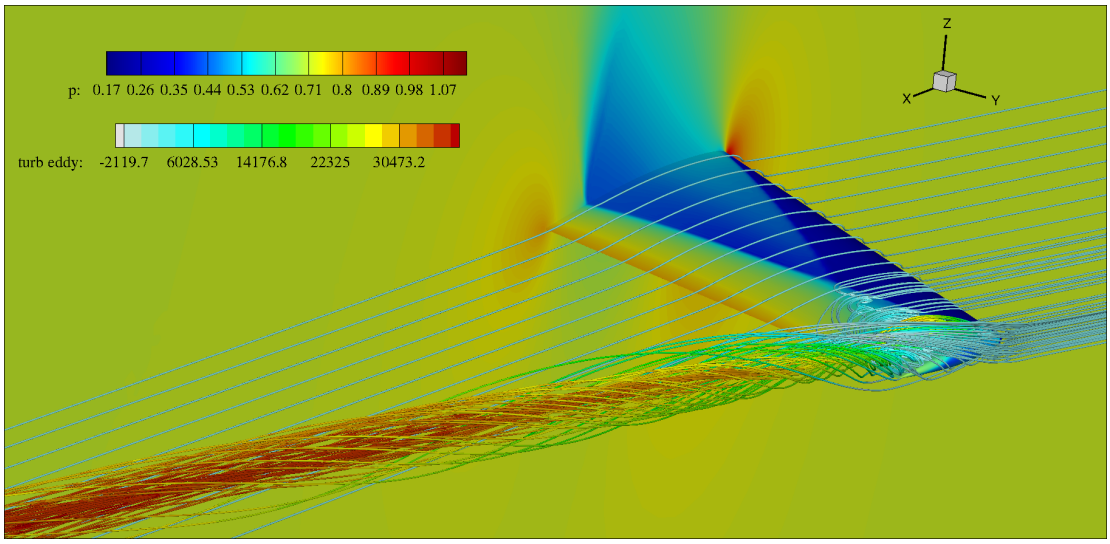

(d) Custom grid 2 (unconverged solution)

Figure 14. Pressure contours and stream lines on the custom grids 1 and 2 for the ONERA M6 wing at Mach number of 0.84, Reynolds number of 14.6 million, and angle of attack of 6.06°.